

Article

Digital Control and Demodulation Algorithm for Compact Open-Loop Fiber-Optic Gyroscope

Lin Chen ¹, Zhao Huang ², Yuzheng Mao ², Biqiang Jiang ^{1,*}  and Jianlin Zhao ^{1,*} 

¹ Key Laboratory of Light Field Manipulation and Information Acquisition, Ministry of Industry and Information Technology, Shaanxi Key Laboratory of Optical Information Technology, School of Physical Science and Technology, Northwestern Polytechnical University, Xi'an 710129, China

² Xi'an Flight Automatic Control Research Institute, Xi'an 710065, China

* Correspondence: bqjiang@nwpu.edu.cn (B.J.); jlzhao@nwpu.edu.cn (J.Z.)

Abstract: With the advantages of small size, low cost, and moderate accuracy, an open-loop fiber-optic gyroscope (FOG) has a wide range of applications around control and automation. For the most cost-sensitive applications, a simple and stable digital algorithm with a reduced control-circuit volume and cost is highly desirable to realize high-precision control of a FOG. In this work, a new algorithm for an open-loop FOG is proposed based on the discrete multi-point demodulation in the sinusoidal modulation period. Utilizing this algorithm, stable control and angular velocity calculation of a gyro are realized with effectively suppressed gyro error. The use of this algorithm greatly reduces the requirements for processing power and simplifies the gyro circuit. Based on this algorithm, a digital FOG with a volume of only $25 \times 20 \times 40 \text{ mm}^3$ achieves a bias instability of less than $0.15^\circ/\text{h}$, an angle random walk (ARW) of less than $0.015^\circ/\sqrt{\text{h}}$, a start-up time of less than 1 s, and a 3 dB bandwidth beyond 160 Hz. This low-cost, compact, and high-performance gyro is sufficient to satisfy the requirements of applications in the navigation and control fields such as unmanned driving.

Keywords: open-loop fiber-optic gyroscope; digital control algorithm; compact; cost-effective



Citation: Chen, L.; Huang, Z.; Mao, Y.; Jiang, B.; Zhao, J. Digital Control and Demodulation Algorithm for Compact Open-Loop Fiber-Optic Gyroscope. *Sensors* **2023**, *23*, 1473. <https://doi.org/10.3390/s23031473>

Academic Editor: Saverio Avino

Received: 29 December 2022

Revised: 21 January 2023

Accepted: 26 January 2023

Published: 28 January 2023



Copyright: © 2023 by the authors. Licensee MDPI, Basel, Switzerland. This article is an open access article distributed under the terms and conditions of the Creative Commons Attribution (CC BY) license (<https://creativecommons.org/licenses/by/4.0/>).

1. Introduction

A fiber-optic gyroscope (FOG) is the core sensor for the navigation, positioning, and attitude control of moving objects [1–3]. According to the difference in the control algorithm, it can be divided into closed-loop and open-loop fiber-optic gyroscopes [4]. Although the accuracy of an open-loop fiber-optic gyroscope is not as good as that of a closed-loop one, it consists of an all-fiber architecture without expensive integrated optical modulators, featuring a small size, low cost, and moderate accuracy. Open-loop gyroscopes have drawn much attention in high-end control fields such as automatic driving and robot control [5]. Much research has been carried out on the optical components, electric circuits, and algorithms to further drive down the cost and size of open-loop fiber-optic gyroscopes, the result of which makes them more competitive than Micro Electromechanical System gyro (MEMS) and low-end closed-loop gyros in the market [6–9]. In terms of hardware circuits and control algorithms, the current research focuses on the realization of a more stable and concise control algorithm to reduce the computational power requirements of the processor. Therefore, it becomes possible to use a simpler hardware configuration to achieve high-precision control of a gyro, thereby reducing the control circuit footprint and cost [10–12].

The conventional open-loop gyroscope algorithm demodulates synchronously the amplitudes of the first, second, and fourth harmonic components of its temporal interference waveform, which requires complex multiple synchronous phase-locked solutions and a powerful convolution processor with a high cost and large footprint [13]. In order to overcome this problem, some researchers have produced a solution of characteristic points in the modulation period [12], which can simplify the algorithm. However, this method

suffers from a low signal-to-noise ratio. In this work, a control demodulation scheme based on discrete multi-point demodulation is proposed to obtain a high signal-to-noise ratio without complicated multiple synchronous phase-locking. This algorithm allows the implementation of a gyro's sampling control, signal demodulation, and error suppression into a compact, low-cost FPGA, avoiding the combination of an FPGA and a digital signal processor (DSP) as in a traditional FOG. The size of our open-loop FOG with this algorithm is only $25 \times 20 \times 40 \text{ mm}^3$, which is about 50% of the size of similar gyros, e.g., the DSP17XX series from KVH Inc. with a dimension of $\phi 45.7 \times 22.9 \text{ mm}^2$. At the same time, the use of a low-arithmetic-power processor significantly reduces the cost of our gyro. This kind of cost-effective and compact gyro provides high performances in bias instability of less than $0.15^\circ/\text{h}$, angle random walk (ARW) of less than $0.015^\circ/\sqrt{\text{h}}$, start-up time of less than 1 s, and 3 dB bandwidth of more than 160 Hz. These characteristics promise that the open-loop FOG with our new demodulation algorithm can find potential applications in many fields, such as automation and control.

2. Demodulation and Control Algorithm

2.1. Demodulation Algorithm

The open-loop optical fiber gyroscope constructed in this work is based on the minimization structure of all fiber-optic gyroscopes, as shown in Figure 1. The light from the broad-spectrum light source (SLED module) passing through the coupler enters the polarizer and spatial filter to ensure the purity of the coherent polarization mode and is divided into two counterpropagating beams in the second coupler. Based on the Sagnac effect, the optical path difference φ_s of the two counterpropagating beams in the fiber coil is proportional to the rotational angular velocity Ω [14],

$$\varphi_s = \frac{2\pi LD}{\lambda c} \Omega, \quad (1)$$

where L is the optical fiber length, D is the diameter of the fiber coil, λ is the central wavelength, and c is the speed of light in vacuum. The returned light is filtered again via the polarizer and then enters the detector. The detected interference light intensity is amplified, sampled, and demodulated via the functional circuit to obtain the Sagnac optical path difference.

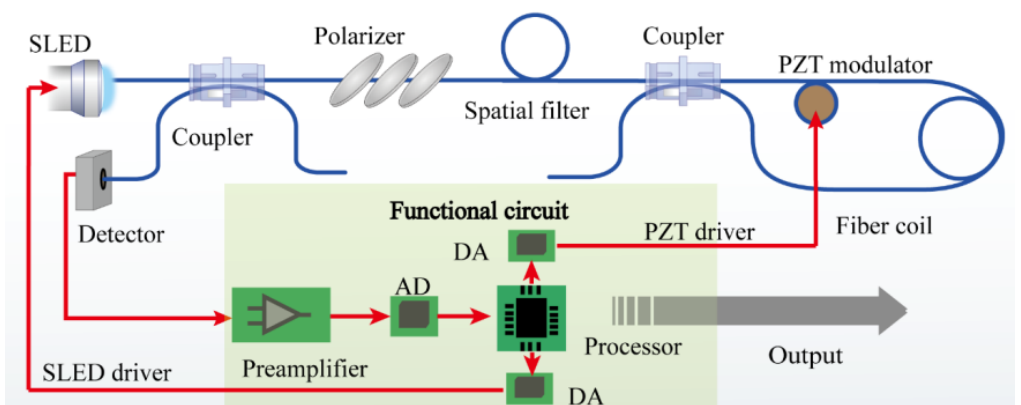


Figure 1. Scheme layout of an open-loop FOG.

A modulator is often used to improve the sensitivity of Sagnac phase-shift demodulation. In comparison with a closed-loop FOG, an open-loop FOG has a great cost advantage due to the use of a lead zirconate titanate piezoelectric ceramics (PZT) modulator, which is only 1/100 the price of the lithium niobate electro-optic modulator used in a closed-loop FOG [15]. Compared with the high-frequency square-wave modulation scheme viable with the use of electro-optical modulators, the bandwidth-limited PZT modulator can only

use a low-frequency sinusoidal modulation scheme, which places higher demands on the demodulation accuracy [16].

Under the sinusoidal modulation scheme, the interference intensity is given by

$$I(\omega t) = I_0 + I_0 \cos(\varphi_{\text{sq}} + \phi_m \sin(\omega t + \tau)), \quad (2)$$

where I_0 is half of the maximum light intensity detected and ω is the angular frequency of modulation. In order to use a low voltage to excite its phase-modulating signal, the PZT is driven close to its resonance frequency. The modulator can only operate efficiently in a small frequency bandwidth of about 5 kHz around its resonance and driving frequencies deviating from the resonance will result in a sharp decay in the PZT oscillation amplitude. Therefore, the effect of multiple harmonics of the PZT is negligible. τ represents the phase delay, which corresponds to the sampling delay for this digital gyro, ϕ_m is the amplitude of phase modulation, and $\varphi_{\text{sq}} = \varphi_s + \varphi_q$, where φ_s is the Sagnac phase shift and φ_q represents the polarization error that cannot be decoupled from the Sagnac phase shift and can only be suppressed with optimized optical devices [17,18].

The interference intensity is converted into a voltage signal with a photo detector followed by a linear preamplifier circuit, as shown in Figure 1, and the amplified voltage signal is sampled evenly with a set sampling frequency, as shown in Figure 2, which is $18 \omega/\pi$ in this work to balance the accuracy and hardware resource requirements. Hence, the sampled discrete signals in a modulation cycle are given by

$$I'(n) = I_0 + I_0 \cos(\varphi_{\text{sq}} + \phi_m \sin((n\pi/18) + \tau)), n = 0, 1, 2 \dots 35 \quad (3)$$

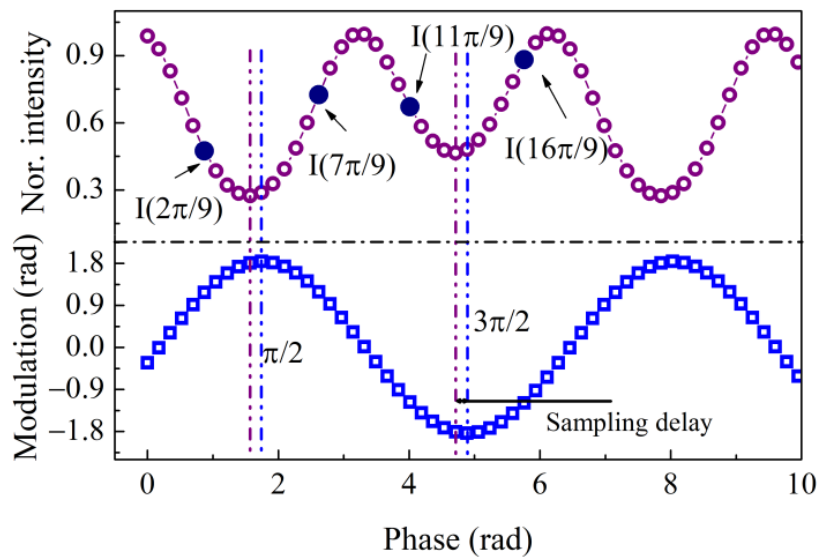


Figure 2. Modulation and discrete sampling of the normalized interference signal.

Define that

$$U = \sum_{n=0}^{35} (I'(n) \sin(n\pi/18)). \quad (4)$$

Since τ represents the sampling phase delay for the digital gyro, which is closed-loop controlled to a very small residual amount compared with the modulated phase, by substituting Equation (3) into Equation (4) and making a first-order approximation for terms containing τ , we obtain

$$\begin{aligned} U &= \sum_{n=0}^{35} (I_0 \sin(n\pi/18)) + \sum_{n=0}^{35} (I_0 \cos(\varphi_{sq} + \phi_m \sin(n\pi/18) + \tau)) \sin(n\pi/18)) \\ &= \sum_{n=0}^{35} ((I_0 \cos \varphi_{sq} \cos(\phi_m \sin(n\pi/18 + \tau) \sin(n\pi/18) - I_0 \sin \varphi_{sq} \sin(\phi_m \sin(n\pi/18 + \tau)) \sin(n\pi/18))) \end{aligned} \quad . \quad (5)$$

By using Bessel function expansion, Equation (5) can be written as

$$\begin{aligned} U \approx & \sum_{n=0}^{35} I_0 \cos \varphi_{sq} \sin(n\pi/18) (J_0(\phi_m) + 2 \sum_{k=0}^{\infty} J_{2k}(\phi_m) \cos 2k(n\pi/18)) (\cos(\phi_m \cos(n\pi/18)\tau) \\ & - \sum_{n=0}^{35} 2I_0 \sin \varphi_{sq} \sin(n\pi/18) \sum_{k=0}^{\infty} J_{2k+1}(\phi_m) \sin((2k+1)(n\pi/18)) (\cos(\phi_m \cos(n\pi/18)\tau) \end{aligned} \quad , \quad (6)$$

where J is the Bessel function of the first kind. By making use of

$$\sum_{n=0}^{35} \sin(n\pi/18) \sin((2k+1)(n\pi/18)) \approx 0, k \neq 0, \quad (7)$$

and

$$\sum_{n=0}^{35} \sin(n\pi/18) \cos(2k(n\pi/18)) \approx 0, \quad (8)$$

and retaining the cumulative non-zero terms, we can obtain

$$U \approx -36I_0 J_1(\phi_m) \cos^2(\phi_m \tau/2) \sin \varphi_{sq}. \quad (9)$$

Therefore,

$$\varphi_{sq} = -\arcsin\left(\frac{U}{36I_0 J_1(\phi_m) \cos^2(\phi_m \tau/2)}\right). \quad (10)$$

From Equations (7) and (8), the main deviation in the derivation of the angular rate comes from the higher harmonic residuals generated by the inner product of the sinusoidal signal generated at the discrete point and the interferometric signal. This error can lead to deviation in the scale factor and nonlinearity in the gyro output, the former of which can be corrected via rate calibration and compensation. Meanwhile, the nonlinear error in the Sagnac phase shift can be suppressed by adding single-cycle sampling points. The sampling rate of 36 points per cycle used in this work is a compromise between the acceptable gyro output accuracy and the limited hardware resources. Nevertheless, our numerical simulation results suggest that the nonlinear error of the gyro can be suppressed with more sampling points per cycle, and linearity within 100 ppm is achievable.

As a result, stable power I_0 , settled modulation amplitude ϕ_m , and smallest possible sampling delay τ are all necessary to precisely obtain the Sagnac phase shift. The control algorithm is described as follows.

2.2. Control of the Synchronous Sampling Delay

In the algorithm, the processor sends commands to the DA to drive the PZT to generate a sinusoidal modulated signal, which is shown in the lower part of Figure 2. The phase modulation is loaded on the interferometric light intensity, and the normalized light intensity is shown in the upper part of Figure 2. The sampling signal is synchronized with the drive signal, but the interference signal lags behind this original sampling signal due to the capacitance of the piezoelectric ceramic and the delay of the processing circuit. In the algorithm, the sampling delay should be precisely controlled to achieve accurate demodulation, and the methods are as follows.

Equally spaced sampling points are determined around the points $\pi/2$ and $3\pi/2$, as shown in Figure 2. With a picking interval ξ , we can determine that

$$\Delta = I(\pi/2 + \xi) - I(\pi/2 - \xi) + I(3\pi/2 + \xi) - I(3\pi/2 - \xi) = 4I_0\tau \sin \xi \cos \varphi_{sq} \sin(\phi_m \cos \xi). \quad (11)$$

Since the values of φ_{sq} and ξ range from $-\pi/2$ to $\pi/2$, $\Delta = 0$ only happens when $\tau = 0$. Therefore, the synchronous sampling delay τ could be controlled with feedback to make $\tau = 0$ by measuring Δ . Choosing the appropriate picking interval ξ can maximize $\Gamma = \sin \xi \sin(\phi_m \cos \xi)$ so as to obtain an optimum sensitivity of feedback control for Δ . With different values of ϕ_m , the variation in Γ as a function of the picking interval is shown in Figure 3. Note that the optimum ξ is between 0.8 and 1, and considering the discreteness of sampling, ξ is set to a value of $5\pi/18$. Thus, τ can be controlled with calculations of the 4 sampling points at $2\pi/9$, $7\pi/9$, $11\pi/9$, and $16\pi/9$. When τ approaches zero, Equation (10) then reduces to

$$\varphi_{sq} = -\arcsin\left(\frac{U}{36I_0J_1(\phi_m)}\right). \quad (12)$$

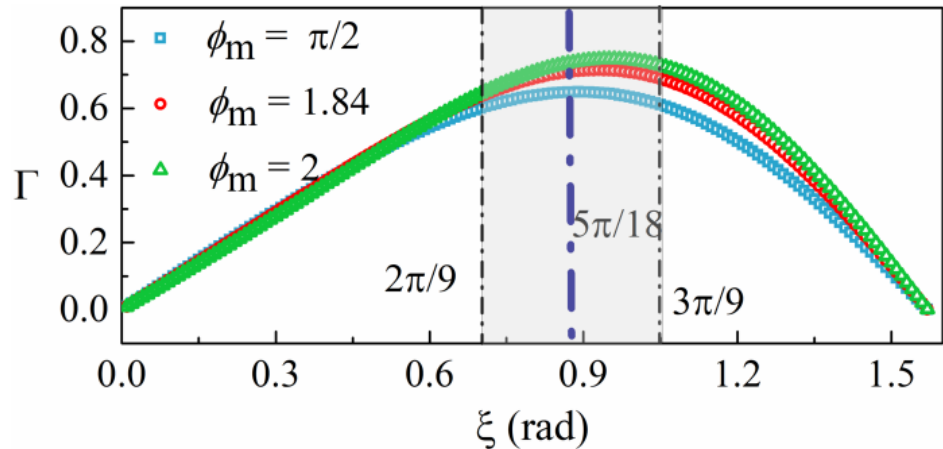


Figure 3. Optimized picking interval for the elimination of the synchronous sampling delay, τ , at different modulation amplitudes.

2.3. Control of the Modulation Amplitude

According to Equation (9), the optimum signal-to-noise ratio (SNR) for U can be obtained when $J_1(\phi_m)$ takes the maximum value, which means that $\phi_m \approx 1.84$ and $J_1(\phi_m) \approx 0.58$. Define that

$$K = (I(\pi/2) + I(3\pi/2))/2 = I_0 + I_0 \cos(\varphi_{sq}) \cos(\phi_m), \quad (13)$$

$$S = (I(3\pi/2) - I(\pi/2))/2 = I_0 \sin(\varphi_{sq}) \sin(\phi_m), \quad (14)$$

$$A = (I(0) + I(\pi))/2 = I_0 + I_0 \cos(\varphi_{sq}), \quad (15)$$

$$B = (I(\pi/6) + I(7\pi/6))/2 = I_0 + I_0 \cos(\varphi_{sq}) \cos(\phi_m/2), \quad (16)$$

$$C = (I(\pi/3) + I(4\pi/3))/2 = I_0 + I_0 \cos(\varphi_{sq}) \cos(\sqrt{3}\phi_m/2). \quad (17)$$

The dynamic range of the open-loop gyro is $(-\pi/2, \pi/2)$, and thus $\cos(\varphi_{sq}) > 0$. Based on Equations (15)–(17), we can determine that

$$M = \frac{A - B}{A - C} = \frac{1 - \cos(\phi_m/2)}{1 - \cos(\sqrt{3}\phi_m/2)}. \quad (18)$$

Equation (18) suggests that if the driving voltage of PZT is controlled to make $|M - 0.385| \leq err_1$ (err_1 is a predefined acceptable control error for PZT, which is 0.0003 in this work), ϕ_m could be controlled to (1.84 ± 0.005) rad.

2.4. Control of Optical Intensity

According to the demodulation algorithm defined by Equation (9), the averaged optical intensity I_0 should be settled to a predefined constant value (i.e., the first derivative equals zero) in the demodulation control process. Consequently, the gyro can realize a stable output as long as the I_0 is closed-loop controlled. Since the SNR of the FOG mainly depends on the shot noise that is proportional to $\sqrt{I_0}$ [18], the gyro's input optical intensity should be increased as much as possible in order to obtain more accurate demodulation results. However, a higher optical intensity of the light source leads to its reduced lifetime and increased relative intensity noise [19] and thus decreased SNR. Therefore, considering both factors, in this work, a moderate optical intensity I_0 corresponding to an optical power of 10 μW is chosen for our gyro. The control process is then given as follows. With $\phi_m = 1.84$ rad, substitute ϕ_m into Equations (13) and (16), and thus,

$$I_0 = (0.606K + 0.266B) / 0.872. \quad (19)$$

The control of optical power can be achieved by changing the drive current of the light source to make $|I_0 - T| \leq err_2$ (err_2 is the predetermined acceptable optical power control error depending on the control accuracy of the SLED, which is 0.005 μW in this work), where T is the target value of the optical power, i.e., 10 μW in this work.

2.5. Suppression of the Bias with a Periodic Flip of Modulation

The rotation speed of the gyro can be derived from Equation (12). However, in the actual implementation process, crosstalk between circuit signals will also cause an error that is independent of the rotation speed and manifested as the zero-bias. Stable zero-bias can be calibrated and removed in a system application [20]. However, this kind of error is often non-stable in most cases, greatly affecting the accuracy of a positioning system.

The traditional approach uses elaborate circuit layouts to isolate and shield all the noise sources [21]. However, this approach requires a larger circuit layout area, which is unsuitable for developing a small-volume open-loop fiber-optic gyroscope. It has been found that most noise results from the gyro's electric source and ground wire [22], which is independent of the modulation polarity. According to Equation (12), because $J_1(\phi_m)$ is an odd function, the error can be easily eliminated by flipping the modulation polarity regularly and changing the output polarity simultaneously. The detailed modulation process is as follows.

The sinusoidal driving waveform of PZT is generated from DA controlled by the FPGA whose clocking is supplied by a crystal oscillator shown in Figure 4a. The exact moment of zero-crossing can be adjusted accurately, which corresponds to the extreme point of the interference signal. The driving voltage applied to the PZT modulator across points A and B is switched periodically between the DA output and the ground. As shown in Figure 4b, each modulation segment lasts for eight full modulation cycles, and the phase of consecutive modulation segments is increased by π , meaning that the modulation polarity of PZT is flipped periodically at the zero-crossing point. This form of modulation pattern not only realizes the modulation inversion but also ensures the continuity of the interference waveform. Data from one cycle each before and after the flipping are discarded during the demodulation process to prevent gyro noise caused by PZT flipping. Considering the bias due to crosstalk, the output of the FOG takes the form of

$$\begin{aligned} \varphi_{sq}(\phi_m) &= -\arcsin\left(\frac{U}{36I_0J_1(\phi_m)}\right) + \varepsilon \\ \varphi_{sq}(-\phi_m) &= \arcsin\left(\frac{U}{36I_0J_1(\phi_m)}\right) + \varepsilon \end{aligned}, \quad (20)$$

where $\varphi_{sq}(\phi_m)$ and $\varphi_{sq}(-\phi_m)$ are the demodulated phases with positive and negative modulation, respectively, and ε is the error due to electric crosstalk. Hence, the bias

due to the crosstalk can be eliminated, and the accurate gyro output can be achieved by synchronously flipping the polarity of the gyro's output according to

$$\varphi_{\text{sq}} = \frac{\varphi_{\text{sq}}(-\phi_m) - \varphi_{\text{sq}}(\phi_m)}{2}. \quad (21)$$

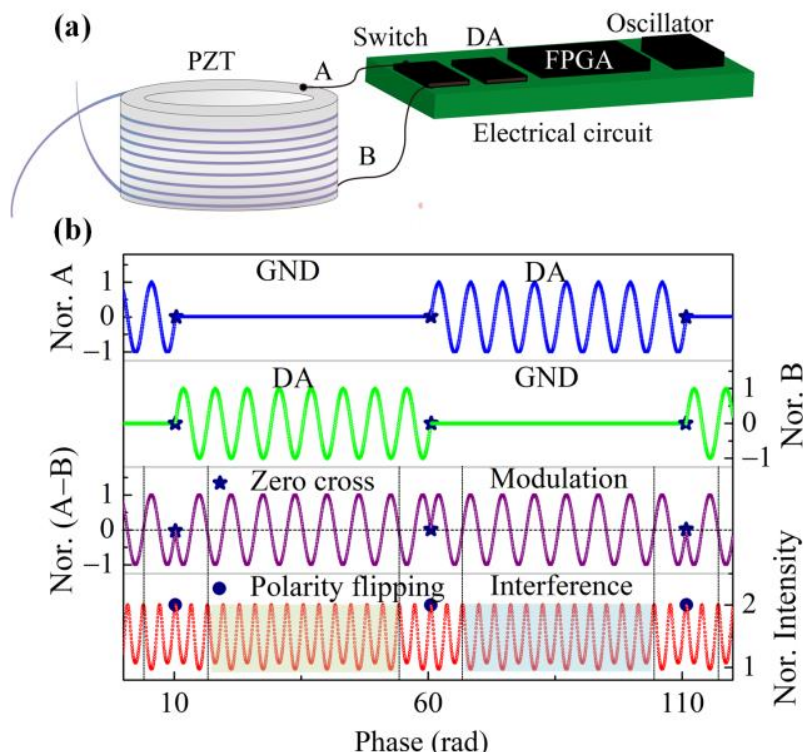


Figure 4. (a) Diagram of PZT control; (b) periodically flipped driving pattern, the modulation generated by the driving, and the corresponding interference signal of the gyro (assuming that the gyro has a Sagnac phase shift of 0.05 rad for clarity).

3. Software, Hardware Implementation, and System Construction

Based on the analysis above, the proposed algorithm uses simple arithmetic operations to replace the traditionally used and more complex multi-frequency convolution algorithm, thereby reducing the requirements for the computing power of the processor. Most open-loop FOGs with digital control [23] use both an FPGA and DSP for signal processing, whereby the FPGA is used to control the sampling timing, and the DSP is used for complex calculation.

In our design, a low-cost Xilinx Spartan-7 FPGA is sufficient for the implementation of all the algorithms. The whole electrical circuit is about half the cost of conventional open-loop FOG products and with a compact footprint of only $35 \times 22 \text{ mm}^2$. The hardware diagram and software process are shown in Figure 4. The FPGA controls the analog-to-digital converter (ADC) to sample the interference light and the digital-to-analog converter (DAC) to achieve the closed-loop feedback of the SLED output power and the phase of the PZT modulator. The computation required by the digital demodulation of the Sagnac phase with bias suppression is also conducted in the FPGA. The timing of the above processes is precisely controlled with a crystal oscillator. The initial values of the control parameters as a function of start-up temperature are determined during the calibration process after the gyro is assembled. They are tabulated and pre-stored in the memory of the gyro's circuit board for the fast retrieval of multiple control parameters at the start-up within the full temperature range [24].

A prototype open-loop FOG, based on the schematic shown in Figure 1, was assembled with the circuit hardware and software configuration as discussed above. An ultra-fine 40 μm polarization-maintaining optical fiber of 200 m long was wound on a ring skeleton with a size of $35 \times 18 \times 22 \text{ mm}^3$ using a quadrupole symmetrical winding method. An in-house packaged miniaturized GaAs SLED light source of a center wavelength of 830 nm was adopted. It was mounted on a heat sink that had thermal contact with the mechanical structure of our open-loop FOG, and no active cooling was applied to it. The output power of the light source can be more than 500 μW under a driving current of 60 mA with a fiber-coupled power of 50 μW . The 2 couplers were in-house developed fused taper-type couplers using the 40 μm polarization-maintaining fiber. The beam-splitting ratio error was less than 5%, and the polarization-maintaining capability was greater than 20 dB. The polarizer was also an in-house developed 45° tiled fiber Bragg grating whose extinct ratio is more than 35 dB [25,26]. A 100 kHz sinusoidal-modulated PZT phase modulator with about 1 m long wrapped fiber was integrated into the system to reduce the size and cost of the FOG. All the optical components and streamlined circuit board with our new algorithm fit into a volume of only $25 \times 20 \times 40 \text{ mm}^3$ to construct the miniaturized open-loop fiber-optic gyroscope, which is shown in Figure 5d.

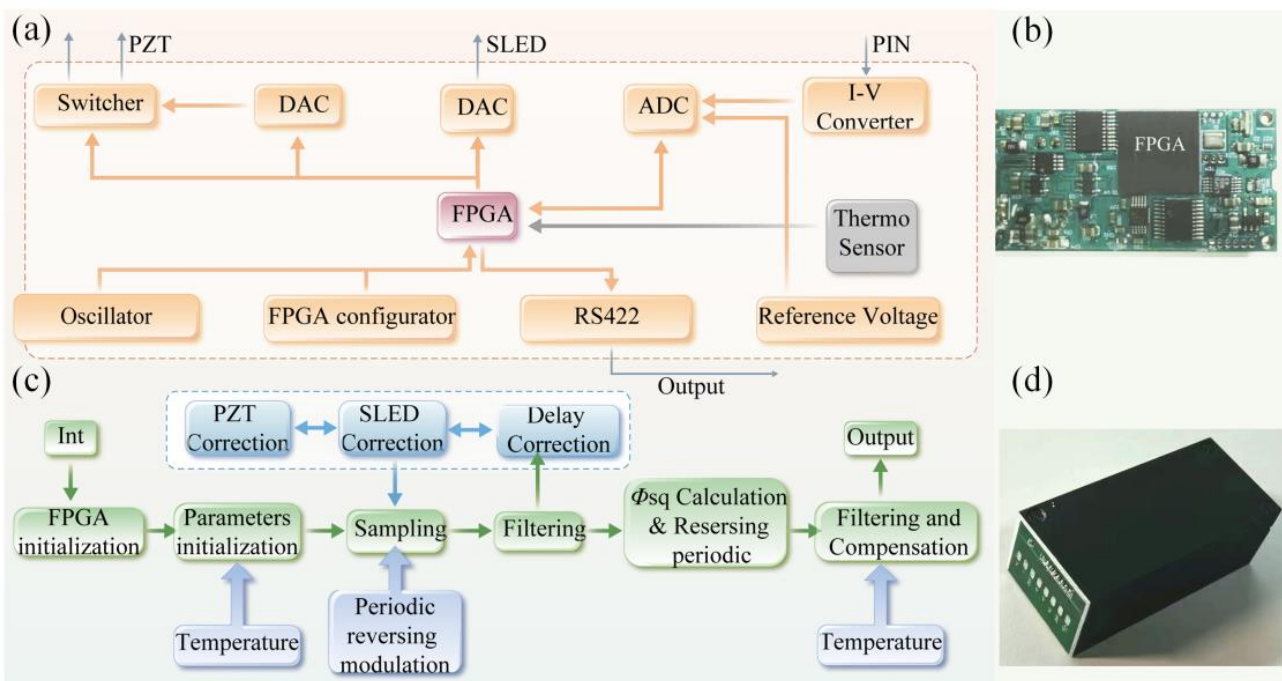


Figure 5. (a) Circuit hardware diagram, (b) picture of the circuit hardware, (c) software process of FOG, and (d) picture of the FOG.

4. Determinations of Gyroscope Performance

Fast start-up is an important metric for a fiber-optic gyro used in the field of control and automation. Prior to gyro performance testing, it is essential to evaluate the start-up process of the control parameters for the new algorithm.

The experimental results show that our proposed control algorithm can control all objectives, including the power of the light source, the PZT modulation phase, and the sampling delay within 0.4 s to reach their steady state, as shown in Figure 6. This means that taking into account the 0.6 s required for FPGA initialization, the gyro start-up time only adds up to less than 1 s.

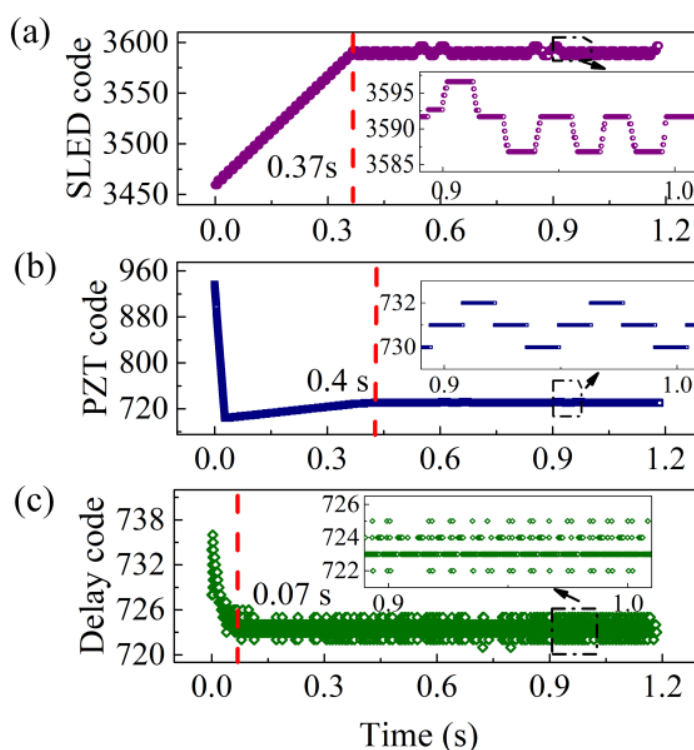


Figure 6. Dynamic control results of (a) SLED, (b) PZT, and (c) sampling delay during the startup process.

The performance of this open-loop FOG prototype is characterized according to the *IEEE 952-2008 protocol*. The test of our FOG was conducted in a Class-10k cleanroom with a temperature of $25 \pm 1^\circ\text{C}$, a humidity of $40 \pm 5\%$, a magnetic field of less than 1 Gauss, and an air pressure of 1 atm. The gyroscope was mounted on a fixed base attached to a separate foundation to isolate the external vibration. The output of this FOG was close to linear with the angular rotation of the test platform on which the FOG was mounted. Figure 7a shows that the scale factor error was less than 200 ppm. Allan variance was used to evaluate the static characteristics of the gyro, i.e., the ARW for white noise and bias instability (B_1) [27]. As shown in Figure 7b, on the Allan variance curve, ARW can be estimated by dividing the value at 1 s by 60 to be $0.012^\circ/\sqrt{\text{h}}$ and B_1 can be calculated by dividing the bottom of the curve by 0.664 to be $0.11^\circ/\text{h}$. To verify the dynamic performance of the gyro, we tested the amplitude–frequency characteristics of the gyroscope with a swing table under different swing frequencies [28]. The FOG had excellent dynamic characteristics with a 3 dB bandwidth of 160 Hz, as shown in Figure 7c, which can meet the application requirements in the field of automatic driving, robot control, etc. [29]. The Gaussian-like decay of the amplitude–frequency curve indicates that the bandwidth of the gyro was mainly limited by the low-pass filter in the algorithm, which can be further improved by optimizing the filter. The effectiveness of the bias elimination algorithm was also verified, as shown in Figure 7d, and after turning on the periodic flip, the gyro's bias decreases from $-55.2^\circ/\text{h}$ to $-8.7^\circ/\text{h}$, which is close to the celestial component of the earth's rotation speed of $-8.4^\circ/\text{h}$ at the test location (Xi'an, Shaanxi Province, China, with its latitude of 34° N). We placed the gyro in reverse (the direction of the sensitive axis changed from pointing to the ground to the sky) and repeated the above experiment. The output of the gyro changed from $-37.5^\circ/\text{h}$ to $7.9^\circ/\text{h}$ after turning on the periodic flip. The earth's rotation speed was eliminated by adding the forward and reverse output together and dividing this sum by two. By periodically flipping its sensitive axis, the gyro gives an output of $-0.25^\circ/\text{h}$, compared with $-46.4^\circ/\text{h}$ obtained without periodic flip.

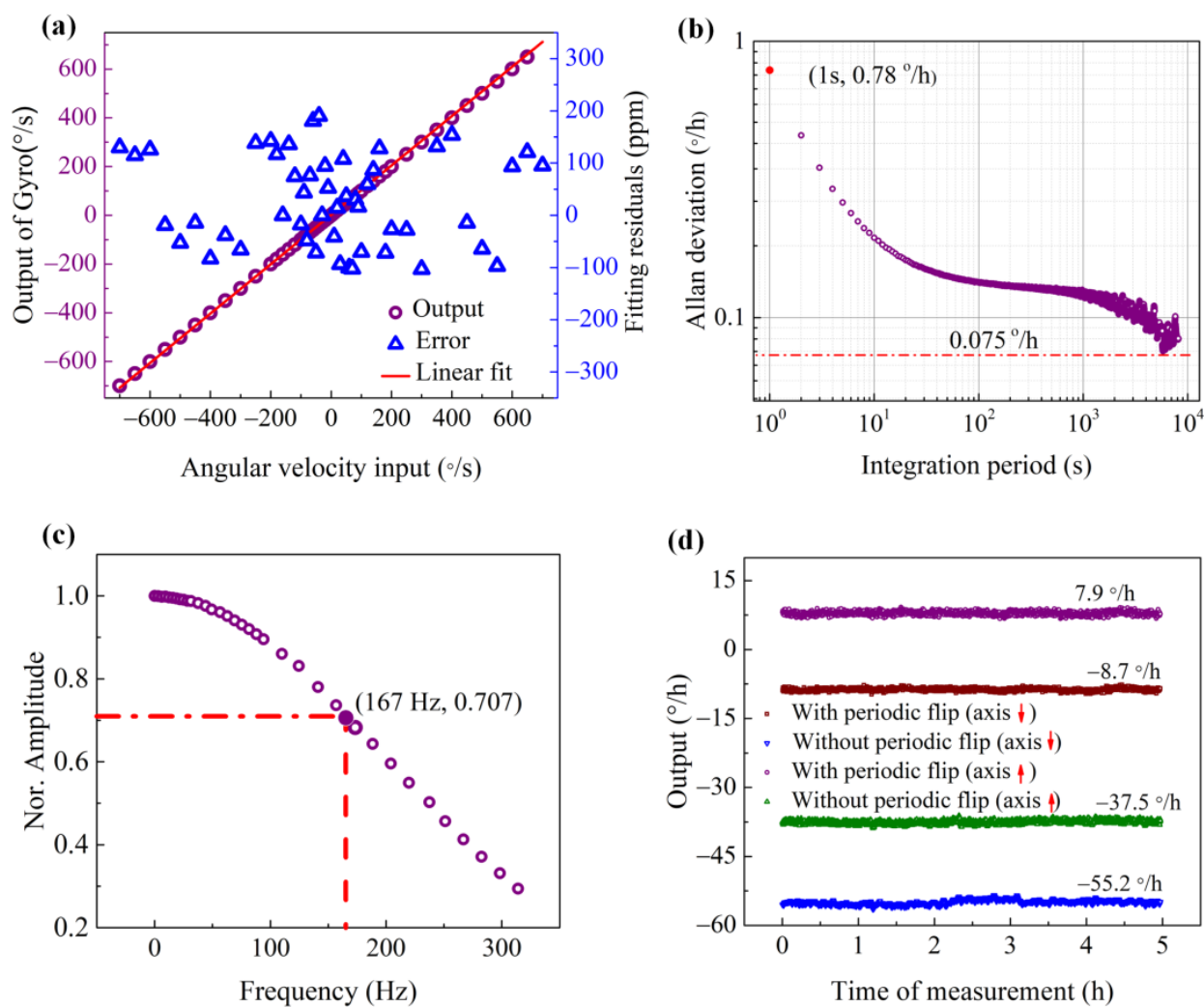


Figure 7. The measured results for our digital open-loop fiber-optic gyroscope. (a) Gyro output at different angular rates, (b) results for Allan variance testing, (c) gyro amplitude-frequency characteristics, and (d) bias comparison with the different algorithms.

According to our experimental results, the open-loop fiber-optic gyro with our new control and demodulation algorithm achieves very good performance. However, our algorithm can be further improved by optimizing its low-pass filter to boost the gyro's 3 dB bandwidth and squeezing more sampling points within a single cycle to reduce gyro noise and suppress nonlinear errors. Currently, 85% of the resource of the low-cost FPGA used in this work has been utilized. The optimization of our above algorithm will possibly have to overhaul the entire structure of the algorithm as well as the implementation of its key functionality to save considerable resources for arithmetic operation.

5. Conclusions

In this work, a new algorithm for an open-loop fiber-optic gyroscope has been proposed. Unlike the traditional resource-intensive synchronous demodulation of multiple harmonic components, our method relies on only a few discrete points on the sinusoidal modulation curve. Based on our algorithm, stable control and angular velocity demodulation of the gyro were both realized. In addition, a periodic flipping modulator driving pattern was proposed and successfully demonstrated to suppress the bias due to the electric crosstalk. Our algorithm greatly reduces the requirements for processing power and simplifies the gyro circuit. As a result, the cost and the volume of the gyro can be greatly reduced. Our prototype digital FOG has a volume of only $25 \times 20 \times 40\text{ mm}^3$, and the comprehensive

testing reveals its bias instability of less than $0.15^\circ/\text{h}$, an ARW of less than $0.015^\circ/\sqrt{\text{h}}$, a start-up time of less than 1 s, and a 3 dB bandwidth beyond 160 Hz. We believe that this kind of performance can meet the navigation needs of autonomous driving vehicles [30] and the control and automation needs of many other applications such as androids.

Author Contributions: This paper was completed by the listed authors. L.C. proposed the digital control algorithm for the FOG and wrote the paper. B.J. proposed the algorithm implementation. J.Z. proposed a scheme for algorithm validation. Z.H. completed the software. Y.M. participated in the experimental data analysis and paper modification. All authors have read and agreed to the published version of the manuscript.

Funding: This research was supported by the National Natural Science Foundation of China (grant no. 61975166).

Institutional Review Board Statement: Not applicable.

Informed Consent Statement: Not applicable.

Data Availability Statement: The data presented in this study are available on request from the corresponding author.

Conflicts of Interest: The authors declare no conflict of interest.

References

1. Clivati, C.; Calonico, D.; Costanzo, G.A.; Mura, A.; Pizzocaro, M.; Levi, F. Large-area fiber-optic gyroscope on a multiplexed fiber network. *Opt. Lett.* **2013**, *38*, 1092–1094. [[CrossRef](#)] [[PubMed](#)]
2. Yao, X.S.; Xuan, H.F.; Chen, X.J.; Zou, H.H.; Liu, X.; Zhao, X. Polarimetry fiber optic gyroscope. *Opt. Express* **2019**, *27*, 19984–19995. [[CrossRef](#)] [[PubMed](#)]
3. Jin, J.; He, J.; Song, N.; Ma, K.; Kong, L. A compact four-axis interferometric fiber optic gyroscope based on multiplexing for space application. *J. Light. Technol.* **2020**, *38*, 6655–6663. [[CrossRef](#)]
4. Udd, E.; Digonnet, M.J.F. *Design and Development of Fiber Optic Gyroscopes*; SPIE Press: Washington, DC, USA, 2019; pp. 35–50.
5. KVH Industries Inc. Guide to comparing gyro and IMU technologies-micro-electro-mechanical systems and fiber optic gyros. *KVH White Pap.* **2014**, 3–5.
6. Zhang, D.; Liang, C.; Li, N. A novel approach to double the sensitivity of polarization maintaining interferometric fiber optic gyroscope. *Sensors* **2020**, *20*, 3762. [[CrossRef](#)]
7. Wu, W.; Zhou, K.; Lu, C.; Xian, T. Open-loop fiber-optic gyroscope with a double sensitivity employing a polarization splitter and Faraday rotator mirror. *Opt. Lett.* **2018**, *43*, 5861–5864. [[CrossRef](#)]
8. Medjadba, H.; Lecler, S.; Simohamed, L.M.; Fontaine, J.; Kiefer, R. An optimal open-loop multimode fiber gyroscope for rate-grade performance applications. *Opt. Fiber Technol.* **2011**, *17*, 546–553. [[CrossRef](#)]
9. Wang, X.; He, C.; Wang, Z. Method for suppressing the bias drift of interferometric all-fiber optic gyroscopes. *Opt. Lett.* **2011**, *36*, 1191–1193. [[CrossRef](#)]
10. Wang, Q.; Yang, C.; Wang, X.; Wang, Z. All-digital signal-processing open-loop fiber-optic gyroscope with enlarged dynamic range. *Opt. Lett.* **2013**, *38*, 5422–5425. [[CrossRef](#)]
11. Bacurau, R.M.; Spengler, A.W.; Dante, A.; Morais, F.J.O.; Duarte, L.F.C.; Ribeiro, L.E.B.; Ferreira, E.C. Technique for suppressing the electronic offset drift of interferometric open-loop fiber optic gyroscopes. *Opt. Lett.* **2016**, *41*, 5186–5189. [[CrossRef](#)]
12. Lu, C.; Zhou, K. A low-cost all-digital demodulation method for fiber-optic interferometric sensors. *Meas Sci Technol.* **2018**, *29*, 105103. [[CrossRef](#)]
13. Gronau, Y.; Tur, M. Digital signal processing for an open-loop fiber-optic gyroscope. *Appl. Opt.* **1995**, *34*, 5849–5853. [[CrossRef](#)] [[PubMed](#)]
14. Lefèvre, H.C. The fiber-optic gyroscope: Challenges to become the ultimate rotation-sensing technology. *Opt. Fiber Technol.* **2013**, *19*(6), 828–838. [[CrossRef](#)]
15. Bergh, R.A. All-single-mode fiber-optic gyroscope with long-term stability. *Opt. Lett.* **1981**, *6*, 502–504. [[CrossRef](#)] [[PubMed](#)]
16. Song, N.; Cai, W.; Song, J.; Jin, J.; Wu, C. Structure optimization of small-diameter polarization-maintaining photonic crystal fiber for mini coil of spaceborne miniature fiber-optic gyroscope. *Appl. Opt.* **2015**, *54*, 9831–9838. [[CrossRef](#)] [[PubMed](#)]
17. Chamoun, J.N.; Digonnet, M.J.F. Noise and bias error due to polarization coupling in a fiber optic gyroscope. *J. Light. Technol.* **2015**, *33*, 2839–2847. [[CrossRef](#)]
18. Ulrich, R. Fiber-optic rotation sensing with low drift. *Opt. Lett.* **1980**, *5*, 173–175. [[CrossRef](#)] [[PubMed](#)]
19. Li, Y.; Ben, F.; Luo, R.; Peng, C.; Li, Z. Excess relative intensity noise suppression in depolarized interferometric fiber optic gyroscopes. *Opt. Commun.* **2019**, *440*, 83–88. [[CrossRef](#)]
20. Zhang, Y.; Guo, Y.; Li, C.; Wang, Y.; Wang, Z. A new open-loop fiber optic gyro error compensation method based on angular velocity error modeling. *Sensors* **2015**, *15*, 4899–4912. [[CrossRef](#)]

21. Li, Z.; Dong, L.; Li, H.; Zhang, J.; Wang, X.; Zhang, H. An analog readout circuit with a noise-reduction input buffer for MEMS microphone. *IEEE Trans. Circuits Syst.* **2022**, *69*, 438–443. [[CrossRef](#)]
22. Bednar, T.; Babusiaak, B.; Labuda, M.; Smetana, M.; Borik, S. Common-mode voltage reduction in capacitive sensing of biosignal using capacitive grounding and DRL electrode. *Sensors* **2021**, *21*, 2568. [[CrossRef](#)] [[PubMed](#)]
23. Napoli, J.; Ward, R. Two decades of KVH fiber optic gyro technology: From large, low performance FOGs to compact, precise FOGs and FOG-based inertial systems. *DGON ISS 2016*, 1–19.
24. Din, H.; Iqbal, F.; Park, J.; Lee, B. Bias-repeatability analysis of vacuum-packaged 3-Axis MEMS gyroscope using oven-controlled system. *Sensors* **2023**, *23*, 256. [[CrossRef](#)] [[PubMed](#)]
25. Jiang, B.; Hou, Y.; Wang, H.; Gan, X.; Li, A.; Hao, Z.; Zhou, K.; Zhang, L.; Zhao, J. Few-layer graphene integrated tilted fiber grating for all-optical switching. *J. Light. Technol.* **2020**, *39*, 1477–1482. [[CrossRef](#)]
26. Jiang, B.; Zhao, J. Nanomaterial-functionalized tilted fiber gratings for optical modulation and sensing. *J. Light. Technol.* **2022**, *1*, 1558–2213. [[CrossRef](#)]
27. Wang, L.; Zhang, C.; Gao, S.; Wang, T.; Lin, T.; Li, X. Application of fast dynamic Allan variance for the characterization of FOGs-based measurement while drilling. *Sensors* **2016**, *16*, 2078. [[CrossRef](#)]
28. Ren, W.; Luo, Y.; He, Q.; Zhou, X.; Deng, C.; Mao, Y.; Ren, G. Stabilization control of electro-optical tracking system with fiber-optic gyroscope based on modified smith predictor control scheme. *IEEE Sens. Lett.* **2018**, *18*, 8172–8178. [[CrossRef](#)]
29. Passaro, V.M.N.; Cuccovillo, A.; Vaiani, L.; De Carlo, M.; Campanella, C.E. Gyroscope technology and applications: A review in the industrial perspective. *Sensors* **2017**, *17*, 2284. [[CrossRef](#)]
30. Vivacqua, R.; Vassallo, R.; Martins, F. A low cost sensors approach for accurate vehicle localization and autonomous driving application. *Sensors* **2017**, *17*, 2359. [[CrossRef](#)]

Disclaimer/Publisher’s Note: The statements, opinions and data contained in all publications are solely those of the individual author(s) and contributor(s) and not of MDPI and/or the editor(s). MDPI and/or the editor(s) disclaim responsibility for any injury to people or property resulting from any ideas, methods, instructions or products referred to in the content.